Arjmandi, A., Majhi, B. B., Mérindol, N., Gélinas, S.-E., dos Santos, K. C. G., Burgos-Holguin, I., Guaitolini, Y. M., Lagüe, P., & Desgagné-Penix, I. (2026). Molecular cloning and functional characterization of tyrosine decarboxylase genes from galanthamine-producing Narcissus pseudonarcissus 'King Alfred.'. Phytochemistry, 251, Article 115017. https://doi.org/10.1016/j.phytochem.2026.115017 CC BY 4.0
Phytochemistry 251 (2026) 115017

Contents lists available at ScienceDirect

Phytochemistry

journal homepage: www.elsevier.com/locate/phytochem

Molecular cloning and functional characterization of tyrosine decarboxylase genes from galanthamine-producing *Narcissus pseudonarcissus* 'King Alfred.'

Arghavan Arjmandi [a], Bharat Bhusan Majhi [a], Natacha Mérindol [a], Sarah-Eve Gélinas [a], Karen Cristine Gonçalves dos Santos [a], Isabella Burgos-Holguin [a], Yasmin Moreto Guaitolini [a], Patrick Lagüe [b], Isabel Desgagné-Penix [a,*]

[a] Department of Biochemistry, Chemistry, Physics and Forensic Science, Université du Québec à Trois-Rivières, Trois-Rivières, Québec, Canada
[b] Department of Biochemistry, Microbiology and Bioinformatics, Université Laval, Québec, Québec, Canada

ARTICLE INFO

Keywords:
Amaryllidaceae alkaloids
Aromatic amino acid decarboxylase
Tyramine biosynthesis
Pyridoxal 5′-phosphate–dependent enzyme
Molecular docking
Gatekeeper enzyme
Specialized metabolism
Amaryllidoideae

ABSTRACT

Tyrosine decarboxylases (TyDCs) are pyridoxal 5′-phosphate–dependent enzymes that catalyze the conversion of L-tyrosine into tyramine, a key entry point for Amaryllidaceae alkaloid biosynthesis. From transcriptome data of *Narcissus pseudonarcissus* 'King Alfred', two full-length TyDC isoforms, *NpTyDC1* and *NpTyDC2*, were identified. In this study, both genes were cloned, heterologously expressed in *Escherichia coli*, and purified for functional characterization. Fluorescent protein tagging indicated nucleocytoplasmic localization of both isoforms. Enzymatic assays coupled with HPLC-MS/MS demonstrated that *Np*TyDC1 exhibits decarboxylase activity with a strong preference for L-tyrosine, producing tyramine as the predominant product. In contrast, *Np*TYDC2 showed no detectable tyrosine decarboxylase activity under the conditions tested, and no tryptophan decarboxylation despite structural features associated with indole decarboxylases but displayed minor activity toward L-phenylalanine. Collectively, these findings establish *Np*TyDC1 as a strong candidate for directing tyrosine into the Amaryllidaceae alkaloid biosynthesis. By integrating computational predictions with biochemical validation, this study provides new insight into the TyDC functional diversity in *Narcissus*.

1. Introduction

The daffodil (*Narcissus spp.*) is the symbol of the Canadian Cancer Society, a noteworthy coincidence given that *Narcissus* species produce a wide array of bioactive alkaloids with documented anticancer activity. As members of the Amaryllidaceae family, *Narcissus* species produce a remarkably diverse group of specialized metabolites, most of which are derived from amino acids such as L-tyrosine and L-phenylalanine. To date, more than 650 Amaryllidaceae alkaloids have been identified, exhibiting a broad spectrum of pharmacological activities. For instance, galanthamine is an acetylcholinesterase inhibitor used to treat mild symptoms of Alzheimer's disease, lycorine displays anticancer properties, and cherylline has antiviral activity (Cortes et al., 2015; Georgiev et al., 2020; Ka et al., 2021). Despite the pharmaceutical importance of these compounds, the biochemical mechanisms governing entry into the Amaryllidaceae alkaloid biosynthetic pathway remain incompletely defined, underscoring the need for detailed functional characterization of the enzymes involved.

All Amaryllidaceae alkaloids can be traced back to a common precursor molecule, 4′-O-methylnorbelladine, formed through the condensation of tyramine and 3,4-dihydroxybenzaldehyde followed by its reduction and 4′-O-methylation (Kilgore et al., 2014, 2016; Koirala et al., 2024; Majhi et al., 2023; Singh et al., 2018; Tousignant et al., 2022). In several Amaryllidaceae species, including *Lycoris aurea* and *Lycoris radiata*, tyramine is produced by a pyridoxal 5′-phosphate (PLP)-dependent non-oxidative tyrosine decarboxylase (TyDC, Fig. 1) (Hu et al., 2021; Wang et al., 2019). TyDC belongs to the group II family of aromatic amino acid decarboxylases (AAADs), which also includes tryptophan decarboxylases (TDC), phenylacetaldehyde synthases (PAAS) and DOPA decarboxylases (DDC) (Sandmeier et al., 1994). Despite high sequence similarity, individual TyDCs often differ in substrate preference and catalytic behaviour (Li et al., 2022; Luaces et al.,

* Corresponding author.
E-mail address: Isabel.Desgagne-Penix@uqtr.ca (I. Desgagné-Penix).

https://doi.org/10.1016/j.phytochem.2026.115017
Received 26 February 2026; Received in revised form 17 June 2026; Accepted 5 July 2026
Available online 6 July 2026
0031-9422/© 2026 The Authors. Published by Elsevier Ltd. This is an open access article under the CC BY license (http://creativecommons.org/licenses/by/4.0/).

2024). Such differences typically arise from subtle variations in the PLP-binding pocket and active-site architecture, which influence substrate positioning and reaction outcome (Torrens-Spence et al., 2020).

Across biological kingdoms, TyDCs carry out distinct roles. In plants, they are often involved in the production of important specialized metabolites. Examples include benzylisoquinoline alkaloids in *Papaver somniferum*, phenylethanoids in *Rehmannia glutinosa*, and health-promoting phenolics in *Olea europaea* (Facchini et al., 1994; Li et al., 2022; Luaces et al., 2024). TyDC activity also contributes to inducible defence responses. In these cases, tyramine is incorporated into the cell wall, where it may help reinforce the tissue during pathogen attack (Kawalleck et al., 1993). Although TyDCs have been characterized in several plant systems, individual isoforms within a given species often exhibit divergent substrate specificities and physiological roles despite high sequence similarity. In many plants, TyDCs are encoded by small multigene families, yet the functional differentiation among isoforms remains poorly resolved, particularly in Amaryllidaceae species where TyDC represents a potential regulatory entry point into alkaloid biosynthesis.

Earlier studies have researched TyDCs in other Amaryllidaceae species by employing transcriptomic analyses, gene cloning, and expression profiling, which uncovered that TyDC is encoded not by a single gene but by a multi-gene family (Hotchandani et al., 2019; Li et al., 2025; Singh and Desgagné-Penix, 2017; Wang et al., 2019). In *Narcissus papyraceus,* multiple isoforms were identified. Each display distinct spatial and temporal expression patterns across organs like bulbs, leaves, and roots. (Hotchandani et al., 2019). However, the biochemical properties, substrate preferences, and structural determinants of individual TyDC isoforms in *Narcissus pseudonarcissus* have not yet been experimentally validated.

In the present study, we addressed this gap by cloning and functionally characterizing two TyDC isoforms from *N. pseudonarcissus* 'King Alfred' (trumpet daffodil). Conserved domain searches, phylogenetic analysis, homology modelling, and molecular docking were combined to predict structural and functional features and identify essential residues within the PLP-binding pocket. Next, these results were experimentally validated using enzymatic assays and kinetic calculations under varying conditions to identify optimal activity parameters. While the *Np*TyDC2 substrate could not be identified, our results revealed that *Np*TyDC1 exhibited activity toward L-tyrosine and L-phenylalanine, consistent with a primary role in directing flux into Amaryllidaceae alkaloid biosynthesis, whereas *Np*TyDC2 does not display detectable tyrosine decarboxylase activity under the conditions tested. Together, these findings establish a biochemical framework for understanding TyDC functional diversification in Amaryllidaceae and provide a foundation for future physiological and metabolic engineering studies.

2. Results and discussion

2.1. Phylogenetic analysis supports that NpTyDC1 is evolutionarily close to other alkaloid-producing plants

The *de novo* transcriptome assembly of *N. pseudonarcissus* cultivar 'King Alfred' yielded 14 TyDC-related transcripts, with two full-length isoforms identified and deposited in GenBank as TyDC-1 (*Np*TyDC1, MF405171) and TyDC-2 (*Np*TyDC2, MF405172) (Singh and Desgagné-Penix, 2017). Protein sequences of TyDC isoforms *Np*TyDC1 and *Np*TyDC2 from *N. pseudonarcissus* were retrieved from public data (UniProt: A0A2H5AIY0 and A0A2H5AIY2, respectively). *Np*TyDC1 comprises 515 amino acids, whereas *Np*TyDC2 is 500 amino acids in length, and the two isoforms share 57% sequence identity. The domain search analysis of these sequences revealed that they belong to the AAT_1 superfamily. Both enzymes shared a PLP binding pocket, and the catalytic residues are, respectively, Lys321 and Lys305 (Fig. S3).

The phylogenetic analysis revealed that *Np*TyDC1 and *Np*TyDC2 cluster into two distinct clades (Fig. 2). *Np*TyDC1 grouped with TyDC sequences from Amaryllidaceae species including *Lycoris*, *Leucojum*, *Narcissus*, and *Crinum*, whereas *Np*TyDC2 clustered with TyDCs from a broader range of monocot species, including sequences from *Acorus*, *Musa* (banana), *Phoenix* (date palm), *Curcuma* (turmeric), *Asparagus*, and *Dendrobium*, and other uncharacterized TyDC2 sequences from Amaryllidaceae species, such as *Leucojum* and *Crinum*. This indicates a potential lineage-specific adaptation for specialized metabolite production, such as in the alkaloid pathway. This clustering is consistent

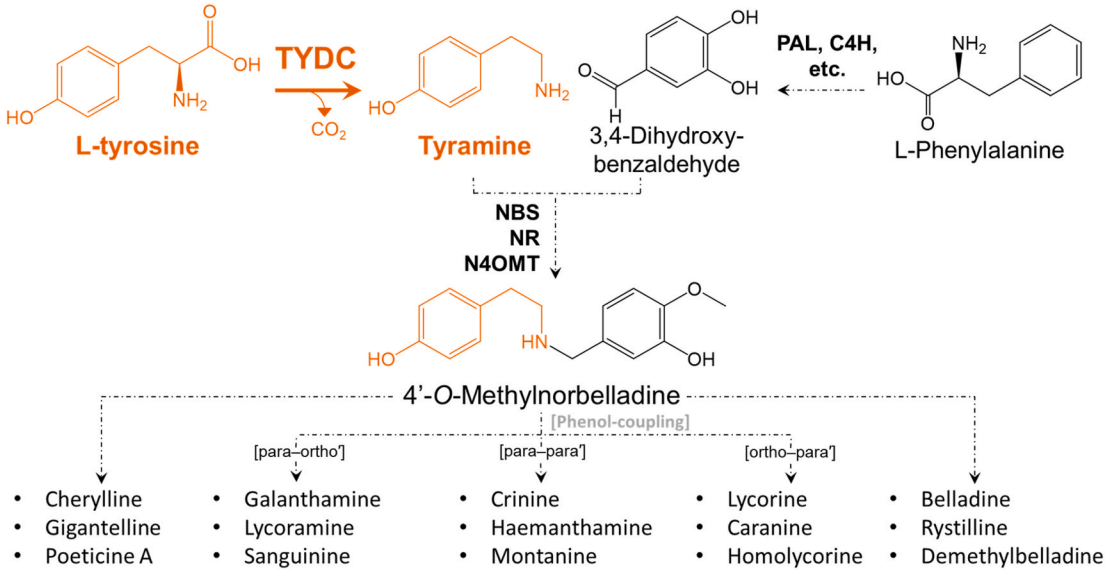


Fig. 1. Simplified overview of Amaryllidaceae alkaloid biosynthesis highlighting the tyrosine decarboxylase (TyDC)–dependent entry step. L-Tyrosine is decarboxylated to tyramine by TyDC with the release of CO_2. In parallel, L-phenylalanine is converted through the phenylpropanoid pathway (PAL, C4H, and downstream enzymes) to yield 3,4-dihydroxybenzaldehyde. Tyramine and 3,4-dihydroxybenzaldehyde condense to form norbelladine via norbelladine synthase (NBS), followed by reduction via norcrausodine/noroxomaritidine reductase (NR) and O-methylation by norbelladine 4′-O-methyltransferase (N4OMT) to produce 4′-O-methylnorbelladine. Subsequent reactions, including phenol-coupling (para–ortho′, para–para′, or ortho–para′), give rise to the major structural classes of Amaryllidaceae alkaloids, including cherylline-, galanthamine-, crinine-, lycorine-, and belladine-type compounds, with representative alkaloids indicated. A solid arrow represents one enzymatic reaction whereas a dashed arrow represents multiple enzymatic steps.

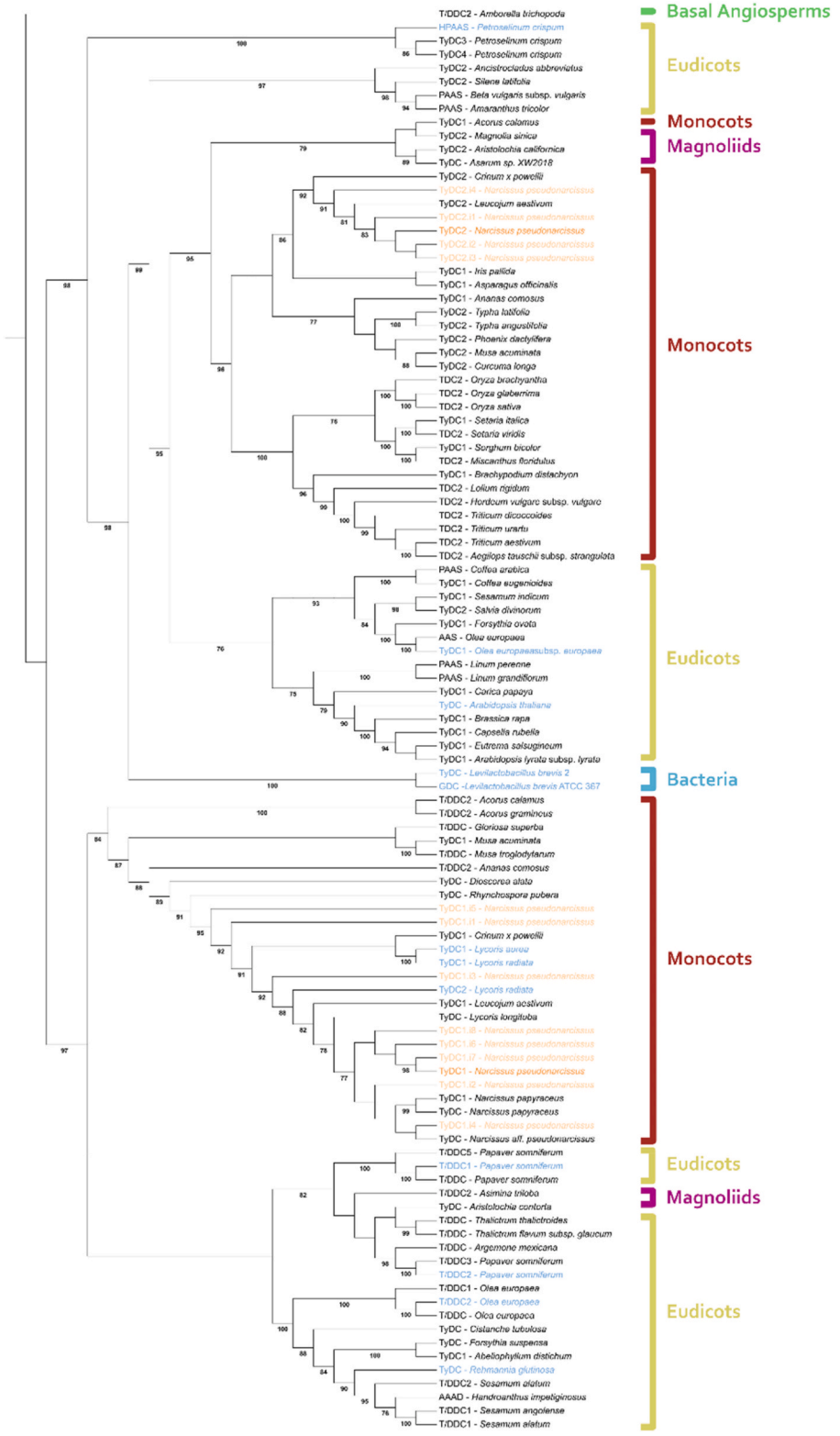


Fig. 2. *Np*TyDC1 clusters with other Amaryllidaceae TyDCs, and *Np*TyDC2 clusters with TyDCs from Amaryllidaceae and other plants. *Np*TyDC1 and *Np*TyDC2 are highlighted with orange. The 12 additional partial TyDC-like sequences from the *N. pseudonarcissus* are shown in light orange. The blue-coloured entries are characterized enzymes. Bootstrap numbers are shown below the branches. (For interpretation of the references to colour in this figure legend, the reader is referred to the Web version of this article.)

with previous phylogenetic studies on Amaryllidaceae TyDCs, where TyDC1-like isoforms form a distinct group associated with galanthamine production (Desgagné-Penix, 2021). For instance, *Lau*TYDC1 from *L. aurea*, which decarboxylates tyrosine to tyramine (Wang et al., 2019), shares high sequence identity and phylogenetic proximity with *Np*TyDC1. By contrast, this clustering implies broader AAAD functions. This divergence mirrors patterns in other alkaloid-producing plants, such as *P. somniferum*, where TyDC isoforms separate into clades for

primary versus specialized metabolism (Facchini et al., 1994). Several of the 12 remaining partial TyDC-like sequences from the *N. pseudonarcissus* grouped within the Amaryllidaceae TyDC1 clade alongside *Np*TyDC1 and characterized *Lycoris* enzymes, while others clustered with *Np*TyDC2 in the broader monocot clade. This distribution suggests that the TyDC gene family in *N. pseudonarcissus* comprises isoforms potentially associated with both specialized and general metabolic functions. Because these sequences are incomplete, their functional contribution could not be further assessed.

2.2. Docking analysis suggests that NpTyDC1 and NpTyDC2 could bind multiple substrates

*Np*TyDC isoforms were modelled as homodimers, with the active site located at the dimer interface and formed by residues from both chain A and B, as in previous structural studies (Torrens-Spence et al., 2020).

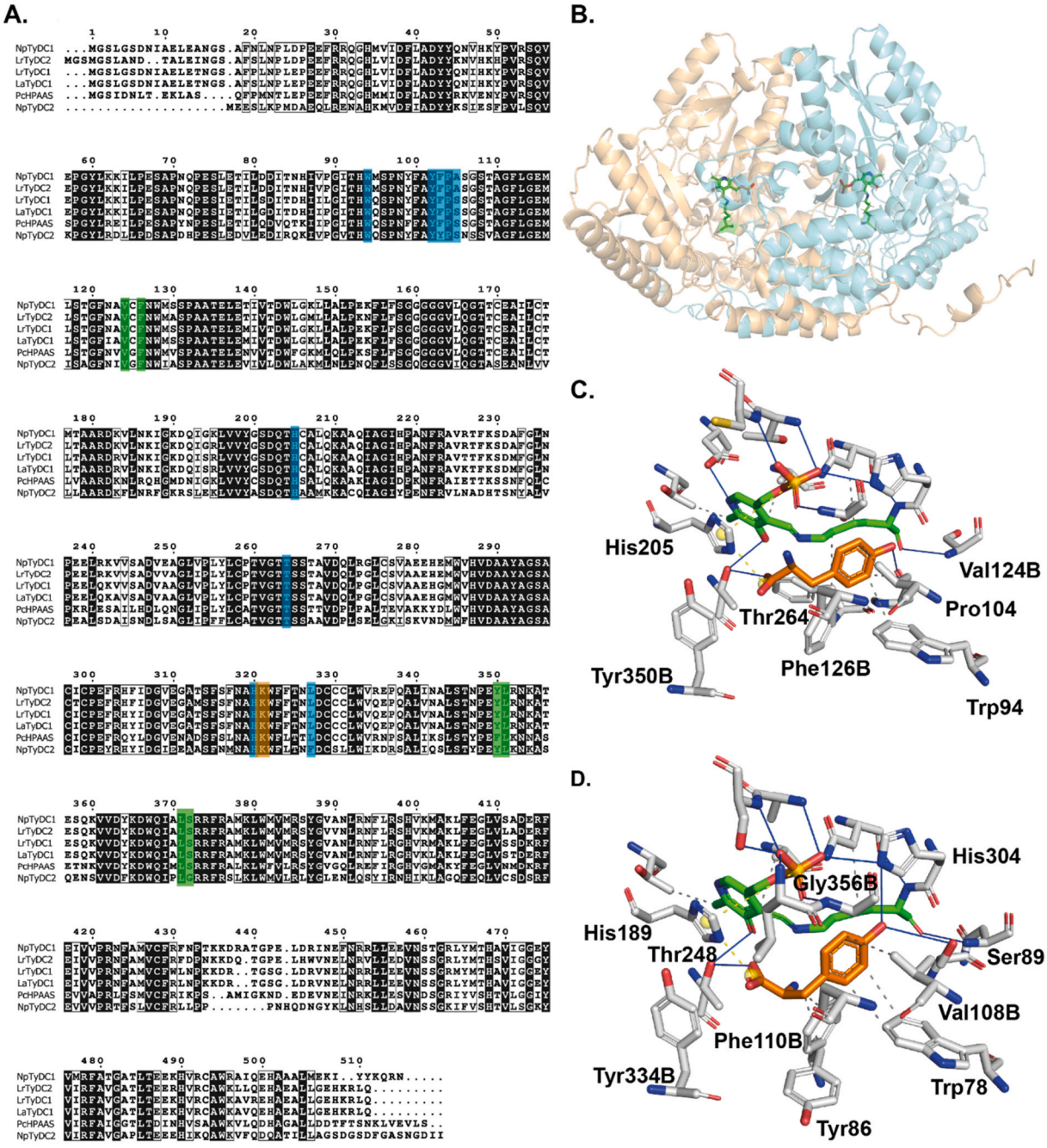


Fig. 3. Conserved active-site architecture of *Np*TyDC1 and *Np*TyDC2 candidates despite key residue differences. A. Multiple sequence alignment of plant TyDCs (and HPAAS from parsley) highlights the conservation of residues that form the *Np*TyDC1 active site. Shaded positions correspond to equivalent amino acids involved in substrate binding and catalysis, as identified by MOE-based pocket detection. Blue positions are from chain A, green positions are from chain B, and the LLP binding site is highlighted in orange. **B.** *Np*TyDC1 dimer predicted folding represented as a cartoon. Chain A is beige, and chain B is turquoise. N′-pyridoxyl-lysine-5′-monophosphate (Lys321-bound PLP) is shown as green sticks. **C.** L-Tyrosine docked inside *Np*TyDC1 active site. Leu355B (not annotated) is displayed bound to Gly356B. **D.** L-Tyrosine docked inside *Np*TyDC2 active site. Interacting residues are shown as grey sticks, LLP is shown as green sticks, and the ligand as orange sticks. H-bonds are shown as blue lines, hydrophobic bonds as dotted grey lines, and salt bridges as dotted yellow lines with yellow spheres. Amino acids from chain B are identified with "B". (For interpretation of the references to colour in this figure legend, the reader is referred to the Web version of this article.)

The models adopted a canonical type II PLP-dependent decarboxylase fold and superposed closely with *Ps*TyDC with an RMSD of 0.363 Å (Fig. 3). Multiple sequence alignment (Fig. 3) showed that residues predicted to constitute the *Np*TyDC1 and 2 active sites are largely conserved across characterized plant TyDCs. LLP consistently interacted with Thr169, Cys170, and Asp289, as in *Cr*TDC, stabilized by pi-stacking with His205 in a closed loop conformation, as in *Ps*TYDC (*e.g.*, Fig. S4). *Np*TyDC1 active-site residues predicted with MOE encompassed conserved aromatic and hydrophobic residues, including Trp94, Phe103, Pro104, Phe126, and His320, consistent with active-site architectures described for other plant AAADs such as *Cr*TyDCs, as well as Tyr350 and Ser372, as reported for *Ps*TyDCs (Table S7). In chain A, all predicted active-site residues are conserved except for the position corresponding to Phe103, which is replaced by Tyr103 in *Np*TyDC2, while phenylalanine is retained at this position in all other present proteins (Fig. S4). Tyr350 is replaced by a Phe in parsley HPAAS, an enzyme previously thought to be a TyDC (Torrens-Spence et al., 2012). The presence of Ser372 at the active site of most TyDCs, which is associated with phenolic amino acid recognition, is replaced by Gly356 in *Np*TyDC2, which is linked instead to indolic substrate recognition in a previous study (Torrens-Spence et al., 2020).

The four ligands, L-tryptophan (−6.9 kCal/mol), L-tyrosine (−6.4 kCal/mol), L-Dopa (−7.0 kCal/mol), and L-phenylalanine (−5.9 kCal/mol) (Table S7), docked in a similar orientation in the active site of *Np*TyDC1, presenting their Cα-carboxyl bond in proximity to the pyridine ring of LLP aldimine (Fig. 3, Fig. S4). The predicted *Np*TyDC1 folding exhibited the least affinity towards L-phenylalanine and the most towards L-DOPA and tryptophan (Table S7, A). Direct interaction with the putative catalytic Tyr350 was detected for L-DOPA, while it was positioned in proximity to the Cα of all ligands. The latter formed a salt bridge with His205 for all ligands, as in *Ps*TyDC. The model is consistent with the catalytic mechanism proposed for *Cr*TDC and *Ps*TyDC. Similar orientation and docking scores were predicted in the *Np*TyDC2 active site (Fig. 3, Fig. S4). The latter displayed predicted higher affinities for L-DOPA and L-tryptophan (−7.5 and −7.4 kcal/mol, respectively) and the lowest score for L-phenylalanine (−6.4 kcal/mol) (Table S7, B). A conserved salt-bridge interaction between the ligands' carboxylate and His189 was observed. Tyr334B (corresponding to Tyr350 in *Np*TyDC1) was located in the vicinity of the ligand tail as well. Although *Np*TyDC2 Gly356B superposed sharply with *Np*TYDC1 Ser372, it induced a conformational change of Leu355B (371B), diving into the active site close to the carboxyl group of the ligand in *Np*TyDC2 (a distance of 3.3 Å in *Np*TyDC2 vs 7.6 Å in *Np*TyDC1), possibly obstructing access to the active site (Fig. 3, Fig. S4). Although docking suggests that *Np*TyDC1 and *Np*TyDC2 could both accommodate the substrates in orientations consistent with their decarboxylation, the difference in the orientation of Leu371/Leu355 could cause steric hindrance to the ligand in *Np*TyDC2 (Fig. S5). The Ser372 to Gly356 substitution in *Np*TyDC2 resulted in Leu355 encumbrance of the active site, possibly reducing efficient binding of phenolic substrates. Although docking predicted that both *Np*TyDC1 and *Np*TyDC2 could accommodate several aromatic amino acids with comparable binding energies, this approach primarily reflects static binding compatibility rather than catalytic competence. In PLP-dependent decarboxylases, small changes in active-site geometry, loop dynamics, or transition-state stabilization can strongly impact reaction outcome without substantially altering predicted binding scores. Our results therefore underscore the limitation of docking alone to infer substrate specificity in AAADs and highlight the necessity of biochemical validation (Torrens-Spence et al., 2013).

2.3. Both NpTyDC1 and NpTyDC2 localize to the cytoplasm and nucleus

To investigate the subcellular localization of *Np*TyDC1 and *Np*TyDC2, their coding sequences from *N. pseudonarcissus* 'King Alfred' were fused in-frame upstream of the *YFP* gene. The resulting *NpTyDC1-YFP* and *NpTyDC2-YFP* constructs were transiently expressed in *Nicotiana benthamiana* leaves via *Agrobacterium tumefaciens*-mediated infiltration, and fluorescence signals were examined by confocal laser scanning microscopy. The cyan fluorescent protein (CFP), which localizes to both the cytoplasm and nucleus (Kruse et al., 2010), was used as a reference marker. As shown in Fig. 4, both *Np*TyDC1-YFP and *Np*TyDC2-YFP fusion proteins were detected in the cytoplasm and nucleus, displaying a localization pattern similar to that of CFP. These findings indicate that *Np*TyDC1 and *Np*TyDC2, which lack predicted signal peptides, are localized to the same nucleocytoplasmic compartment of the cell. This pattern matches what we expected for soluble aromatic amino acid decarboxylases. As a result, neither protein is sent to the secretory pathway or to a membrane-bound compartment. Our finding is consistent with the cytoplasmic localization reported for the *Arabidopsis* tyrosine decarboxylase *At*TyrDC (Lehmann and Pollmann, 2009). Demonstrating that a nucleocytoplasmic location is a shared feature of plant TyDCs. Furthermore, our result agrees with the localization of the downstream enzymes of the pathway. Norbelladine synthase (NBS) and noroxomaritidine/norcraugsodine reductase (NR) both localize to the cytoplasm and the nucleus (Majhi et al., 2023). These two enzymes use the tyramine that TyDC produces. Their shared location with *Np*TyDC1 seems to place the start of the pathway and its first committed steps in the same soluble compartment.

2.4. NpTyDC1 exhibits high substrate sctpecificity for L-tyrosine compared to NpTyDC2

To compare the catalytic efficiencies of *Np*TyDC1 and *Np*TyDC2, we expressed the enzymes in *E. coli* (The SDS-PAGE results are shown in Fig. S6) and measured the standard area ratio of products (tyramine, phenylethylamine, tryptamine, and dopamine) generated from their respective substrates (L-tyrosine, L-phenylalanine, L-tryptophan, and L-DOPA) in enzymatic assays. Product formation was significantly impacted by the combined influence of enzyme isoform, substrate identity, and assay condition. (Table 1, Table S8).

For L-tryptophan and L-DOPA, neither isoform produced detectable tryptamine or dopamine, respectively. However, both enzymes generated phenylethylamine above background when phenylalanine was used as a substrate ($p < 0.001$), although to different extents. There was a 2.4-fold increase in L-phenylalanine conversion for *Np*TyDC1 compared to *Np*TYDC2 ($p < 0.001$). Because tyramine and phenylethylamine differ in their UV detector response factors relative to the internal standard, the ISTD-normalized area ratios for these two products cannot be directly compared within the same enzyme; only comparisons of the same product across the two isoforms are valid. Interestingly, *Np*TyDC1 produced tyramine, the direct precursor of Amaryllidaceae alkaloid biosynthesis, at levels well above those of both controls, with an average product formation of 0.15 based on standard area ratio ($p < 0.001$), confirming strong enzymatic activity. *Np*TyDC2 showed no detectable conversion of substrate with a standard ratio of 0.00053 for the product. In conclusion, *Np*TyDC1 catalyzes the decarboxylation of L-tyrosine under the assay conditions. In contrast, *Np*TyDC2 shows detectable activity toward phenylalanine and no detectable tyrosine decarboxylation. Neither isoform converts tryptophan or L-DOPA *in vitro*. Together, these results show clear functional divergence between the two TyDC isoforms, with *Np*TyDC1 uniquely positioned to channel L-tyrosine toward the alkaloid pathway. This selectivity aligns partially with Amaryllidaceae TyDCs like *Lau*TYDC1 from *L. aurea*, which prefers L-tyrosine over L-DOPA, but the latter shows no L-phenylalanine activity (Wang et al., 2019). Similarly, *Lr*TyDC from *L. radiata* exhibits high tyrosine specificity, correlating with galanthamine levels (Hu et al., 2021). TyDCs from other plants decarboxylate both tyrosine and L-DOPA but not L-phenylalanine. For example, olive (*O. europaea*) *Oe*TDCs and *R. glutinosa Rg*TyDC2 both prefer tyrosine but also accept L-DOPA (Li et al., 2022; Luaces et al., 2024). In *N. pseudonarcissus* 'King Alfred', *Np*TyDC1 carries the expected structural signatures of phenolic substrate recognition (Torrens-Spence et al., 2020), and is the only

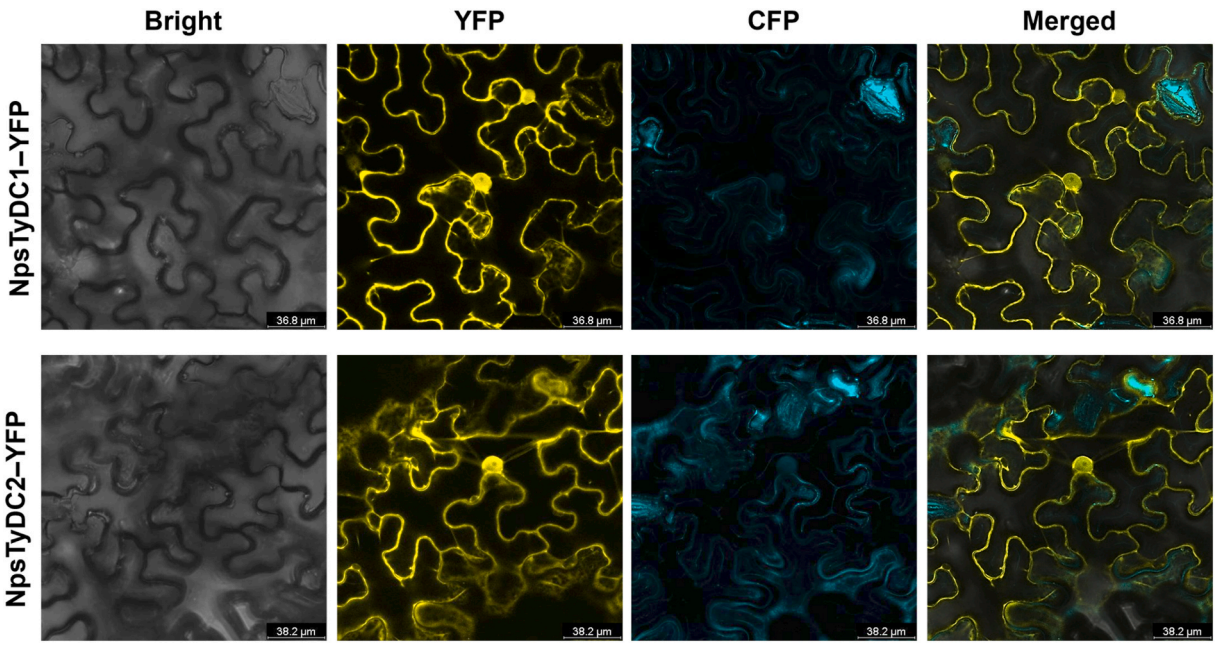


Fig. 4. Subcellular localization of *Np*TyDC1 and *Np*TyDC2 in *Nicotiana benthamiana* epidermal cells. Both *Np*TyDC1 and *Np*TyDC2 localize to the cytoplasm and nucleus. The indicated YFP fusion proteins were co-expressed with cyan fluorescent protein (CFP) in *N. benthamiana* leaves via *Agrobacterium tumefaciens*-mediated transient transformation. Forty-eight hours post-infiltration, fluorescence was observed in epidermal cells using confocal laser scanning microscopy. Bright-field, chlorophyll autofluorescence, yellow fluorescent protein (YFP), cyan fluorescent protein (CFP), and merged fluorescence images are shown. Scale bars are indicated in the images. (For interpretation of the references to colour in this figure legend, the reader is referred to the Web version of this article.)

Table 1
Comparison of product formation by *Np*TYDC1 and *Np*TYDC2 based on standard area ratios relative to the internal standard papaverine.

Substrate	Enzyme	Product	Average ± Std. Deviation[a]
L-Tyrosine	*Np*TyDC1	Tyramine	0.15 ± 0.02
	*Np*TyDC2		0.00053 ± 0.00001
L-Tryptophan	*Np*TyDC1	Tryptamine	0.004 ± 0.001
	*Np*TyDC2		0.0036 ± 0.0003
L-DOPA	*Np*TyDC1	Dopamine	0.024 ± 0.002
	*Np*TyDC2		0.045 ± 0.004
L-Phenylalanine	*Np*TyDC1	Phenylethylamine	0.25 ± 0.03
	*Np*TyDC2		0.10 ± 0.02

[a] Values represent HPLC–DAD peak area ratios normalized to the internal standard (papaverine) and are provided for qualitative comparison of substrate conversion. Due to differences in UV absorption and detector response factors between products, area ratios are not directly comparable across different substrates.

characterized isoform catalyzing L-tyrosine decarboxylation. Although the enzyme also accepts L-phenylalanine, the biological significance of this activity remains unclear, as phenylethylamine is not a known intermediate in Amaryllidaceae alkaloid biosynthesis. No L-tryptophan decarboxylation was detected in enzymatic assays under the tested conditions, but we cannot rule out that *Np*TyDC2 may instead recognize a different indole substrate, not included in the present assays. The lack of tryptophan decarboxylation differentiates *Np*TyDC2 from *Cr*TDC in *Catharanthus roseus*, which produces tryptamine for indole alkaloids (Torrens-Spence et al., 2020). *Np*TyDC2 is a divergent AAAD-like isoform, consistent with its phylogenetic clustering, suggesting a role in primary metabolism instead. *Np*TyDC2 retains all canonical features of PLP-dependent AAADs, including conserved catalytic residues and a well-defined active site, and is broadly conserved across monocots. This suggests that *Np*TyDC2 likely acts on alternative substrates or operates under physiological contexts not captured in the present *in vitro* assays, such as stress-related or developmental regulation, rather than contributing directly to Amaryllidaceae alkaloid biosynthesis. Future studies using broader substrate libraries or *in planta* perturbations will be required to clarify its physiological role. In addition, longer read transcriptome or genome analyses (or RACE) will help resolve the functional contributions of the remaining 12 incomplete TyDC sequences to tyramine biosynthesis.

2.5. Optimization of enzymatic assay conditions for NpTyDC1

Since only *Np*TyDC1 exhibited tyramine production, we continued the subsequent optimization assay focusing exclusively on this enzyme. For temperature (Fig. 5, A), kinetic characterization revealed an optimal temperature of approximately 37 °C, with activity rising from low levels at 20 °C and declining slowly at higher temperatures. For enzyme quantity (Fig. S7), tyramine production increased until maximum activity was observed at 30 ng (Table S9).

We next evaluated the impact of reaction duration (Fig. S8). Tyramine production by *Np*TyDC1 increased progressively with reaction duration, with significant overall differences (Table S10). Substrate conversion increased at short assay durations, reached a maximum at intermediate times (around the 80-min mark), and then reached a plateau. In conclusion, these findings show that *Np*TyDC1 activity is time-dependent, increasing during the early phase of the reaction and peaking at intermediate durations. After measuring product formation in different concentrations of substrate available, tyramine production by *Np*TyDC1 increased in a concentration-dependent manner, with highly significant overall differences ($p < 0.001$). *Np*TyDC1 optimal temperature was 37 °C, similarly to *Oe*TDCs (40 °C) but lower than *Lau*TYDC1 in Wang et al., which was 50 °C. (Luaces et al., 2024; Wang et al., 2019). Enzyme concentration assays showed saturation at 30-60 ng. Increasing enzyme abundance beyond this range did not increase product formation because substrate availability was fixed under the assay conditions. Reaction duration indicated accumulation peaking at 80-160 min, suggesting turnover limits or product inhibition, consistent with *Lb*TDC assays (Zhu et al., 2016).

We propose that TyDC functional divergence within Amaryllidaceae is consistent with adaptation to temperatures. Ptak et al. showed that

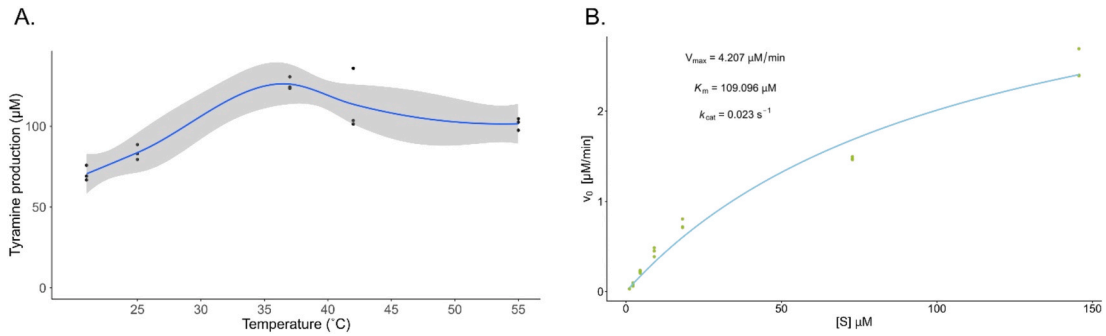


Fig. 5. Kinetic characteristics of *Np*TyDC1. **A. Tyramine production (mM) by *Np*TyDC1 varied with temperature (°C).** 95% Confidence level calculated using 3 replicates. **B. Michaelis-Menten kinetics of *Np*TyDC1**, plotting initial velocity (v_0, μM/min) against L-tyrosine concentration ([S]μM), with fitted curve and annotated parameters. Kinetic analysis was performed at 37 °C with 30 ng of enzyme and a reaction duration of 80 min. V_{max} was projected but not achieved under these conditions.

cold stress (15 °C) causes TyDC expression and the buildup of specialized metabolites in *Leucojum aestivum* cultures grown *in vitro* (Ptak et al., 2026). Together, these observations are consistent with a role for TyDC isoforms in responding to temperature-associated physiological constraints, although this hypothesis remains speculative.

Initial velocity values (v_0) were calculated and used as input for nonlinear regression analysis, resulting in a K_m of 109.1 μM for *Np*TyDC1 (Fig. 5, B). The reaction is projected to reach a maximal rate of 4.207 μM/min (0.23 nkat/mg), as V_{max} was not achieved under the tested conditions. This projected value was then used to derive a turnover number of 0.023 s^{-1} based on the enzyme concentration in the assay. *Np*TyDC1 functions as a tyrosine decarboxylase that converts L-tyrosine to tyramine. The enzyme shows specificity for L-tyrosine and displays consistent kinetic behaviour under the assay conditions, supporting its role as an aromatic amino acid decarboxylase.

Comparison of kinetic parameters with the phylogenetic reconstruction shows that evolutionary relatedness often aligns with enzyme behaviour, but not in a strictly linear manner (Table 2). *Np*TyDC1, characterized in this study, exhibits substrate affinity values that fall within the small range defined by closely related *Lycoris* enzymes as in the phylogenetic tree (Fig. 2). Its K_m of 109 μM lies between that of *Lr*TyDC2 at 60 μM and *Lr*TyDC1 at 390 μM, while *Lau*TyDC1 displays a higher K_m of 602 μM, consistent with its slightly more distant placement in the phylogeny. Catalytic turnover among these enzymes remains uniformly low. *Np*TyDC1 shows a calculated *kcat* of 0.02337 s^{-1}, closely matching *Lr*TyDC2 at 0.03199 s^{-1} and *Lr*TyDC1 at 0.03817 s^{-1}, whereas *Lau*TyDC1 exhibits a moderate increase to 0.2664 s^{-1}. Maximal velocities follow the same constrained pattern, ranging from 0.23 nkat mg^{-1} for *Np*TyDC1 to 0.44–0.53 nkat mg^{-1} for *L. radiata* enzymes, with *Lau*TyDC1 reaching 3.19 nkat mg^{-1} (Hu et al., 2021; Wang et al., 2019).

Rather than reflecting inefficiency, the low catalytic turnover of *Np*TyDC1 is consistent with a gatekeeping role at the entry point of Amaryllidaceae alkaloid biosynthesis, where tight regulation of tyramine availability may be critical to downstream pathway control. Enzymes catalyzing committed steps in specialized metabolism often operate under constrained kinetic regimes, with pathway flux regulated primarily through enzyme abundance, localization, or activation rather than maximal catalytic capacity. In this context, the kinetic properties of *Np*TyDC1 align with its proposed role in regulating access to the alkaloid biosynthetic network rather than sustaining high-flux primary metabolism.

We calculated catalytic efficiencies (*kcat*/K_m) for the enzymes in

Table 2
Comparison of different aromatic amino acid decarboxylases that have been characterized using L-tyrosine as a substrate. The values in blue have been determined by either a unit conversion or have been calculated based on the data available in each corresponding article. The detailed table with all the calculations is in Table S11. All values have been converted to identical units to facilitate the comparisons. Only the entries for which all values were present or could be calculated were kept in the table.

Organism	Enzyme/ Isoform	K_m (μM)	calculated *kcat* (s^{-1})	*kcat* (s^{-1})/K_m (μM)	V_{max} (nkat/ mg)	Molecular weight (kDa)	Reaction volume (μL)	Reference
Lycoris radiata	*Lr*TyDC2	60	0.03199	0.00053317	0.44	72.7	100	Hu et al. (2021)
Narcissus pseudonarcissus	***Np*TyDC1**	**109**	**0.02337**	**0.0002144**	**0.23**	**100**[a]	**100**	**This study**
Rehmannia glutinosa	*Rg*TyDC2	250	0.15	0.0006	2.68	56.05	250	Li et al. (2022)
Lycoris radiata	*Lr*TyDC1	390	0.03817	9.7872E-05	0.53	72.7	100	Hu et al. (2021)
Petroselinum crispum	*Pc*AAS	460	1.06	0.00230435	18.62	57	100	Torrens-Spence et al. (2012)
Lactobacillus brevis IOEB 9809	TDC	580	0.134	0.00023103	1.92	70	2000	Moreno-Arribas and Lonvaud-Funel (1999)
Lactobacillus brevis CGMCC 1.2028	*Lb*TDC	590	343.1	0.58152542	2452	70	1000	Zhang and Ni (2014)
Lycoris aurea	*Lau*TyDC1	602	0.2664	0.00044252	3.19	83.5	150	Wang et al. (2019)
Lactobacillus brevis (Zhu et al., 2016)	*Lb*TDC	630	124.8	0.19809524	1783	70	1000	Zhu et al. (2016)
Lactobacillus brevis ATCC 367	TDC	670	0.077	0.00011493	1.1	70	2000	Moreno-Arribas and Lonvaud-Funel (1999)
Arabidopsis thaliana	*At*TyrDC	745	3.99	0.0053557	61.35	65	300	Lehmann and Pollmann (2009)
Papaver somniferum	*Ps*TyDC1	1000	3.36E-08	3.36E-11	0	57	1000	Facchini and De Luca (1994)
Papaver somniferum	*Ps*TyDC2	1002	7.08E-09	7.0659E-12	0	59	1000	Facchini and De Luca (1994)
Olea europaea	*Oe*TDC2	1290	23.98	0.01858915	161.5	56.4	200	Luaces et al. (2024)
Olea europaea	*Oe*TDC1	1900	12.79	0.00673158	187.7	56.3	200	Luaces et al. (2024)

[a] The molecular weight for *Np*TYDC1 of 100 kDa includes the MBP-tag which is of approximately 40-42 kDa.

Table 2. These values support our interpretation. They also place *Np*TyDC1 within the wider kinetic range of characterized AAADs. *Np*TyDC1 shows a low catalytic efficiency of about 2.1×10^{-4} μM^{-1} s^{-1}. This value is close to that of its nearest phylogenetic relatives. The *Lycoris* enzymes cluster in the same low range (*Lr*TyDC2, ~5.3×10^{-4}; *Lau*TyDC1, ~4.4×10^{-4}; *Lr*TyDC1, ~9.8×10^{-5} μM^{-1} s^{-1}). This narrow range indicates that *Np*TyDC1 is kinetically typical of tyrosine decarboxylases linked to specialized metabolism in this lineage, once we consider affinity and turnover together. On the other hand, enzymes tied to higher-flux or primary metabolism appear far more efficient. Their catalytic efficiencies are greater by one to several orders of magnitude. These include the plant decarboxylases of *O. europaea* (~6.7×10^{-3} to 1.9×10^{-2} μM^{-1} s^{-1}) and *A. thaliana* (~5.4×10^{-3} μM^{-1} s^{-1}). The bacterial *L. brevis* enzymes are higher still (~2.0×10^{-1} to 5.8×10^{-1} μM^{-1} s^{-1}), consistent with sustained tyramine production in primary metabolism. The *P. somniferum* TyDCs fall at the opposite extreme (~10^{-11} to 10^{-12} μM^{-1} s^{-1}), in line with their negligible activity on L-tyrosine. As a result, the low catalytic efficiency of *Np*TyDC1 mirrors its low turnover. This pattern seems consistent with a gatekeeping role at the entry point of Amaryllidaceae alkaloid biosynthesis, where tyramine supply might be controlled through tight kinetic regulation rather than high catalytic throughput.

TyDC1 activity in *N. pseudonarcissus* 'King Alfred' differs fundamentally from that observed in plant systems that are estimated to operate at higher flux, such as *O. europaea*, based on their kinetic characteristics. Comparison with enzymes from *O. europaea* indicates that *Np*TyDC1 operates under kinetic constraints that restrict catalytic activity. These constraints could prevent high-flux tyramine biosynthesis even when substrate affinity is preserved. So, *Np*TyDC1 functions as a tightly regulated, low-output enzyme rather than a bulk metabolic TyDC like in *O. europaea* TyDC1 and TyDC2, where the *kcat* values reach 23.98 s^{-1} and 12.79 s^{-1}, respectively. This increase is also mirrored by their V_{max} (Li et al., 2022; Luaces et al., 2024). TyDCs from *P. somniferum* display the most constrained catalytic profiles in the dataset. Both *Ps*TyDC1 and *Ps*TyDC2 exhibit high K_m values of 1000 and 1002 μM, placing them among the lowest-affinity enzymes examined. Their catalytic turnover is several orders of magnitude lower than all other entries, with *kcat* values of 3.36×10^{-8} s^{-1} and 7.08×10^{-9} s^{-1}, and V_{max} values of 5.90×10^{-7} and 1.20×10^{-7} nkat mg^{-1}, respectively (Facchini and De Luca, 1994).

Bacterial TyDCs define a distinct kinetic regime. Although their K_m values overlap with those of plant enzymes, ranging from 580 to 670 μM, their catalytic turnover exceeds all plant values by orders of magnitude. *Lactobacillus brevis* CGMCC 1.2028 r*Lb*TDC reaches a *kcat* of 343.1 s^{-1}, while the TyDC from a subspecies of *L. brevis* reaches 124.8 s^{-1}, consistent with sustained high-flux activity typical of primary metabolic pathways. Correspondingly, V_{max} values of 2451.67 and 1783 nkat mg^{-1} dwarf those observed in plant systems, including the highly active *O. europaea* enzymes. Other *L. brevis* strains show lower but still elevated V_{max} values of 1.92 and 1.1 nkat mg^{-1}, underscoring strain-level variability within a broadly conserved metabolic function (Moreno-Arribas and Lonvaud-Funel, 1999; Zhang and Ni, 2014; Zhu et al., 2016). This suggests that these bacteria may require tyramine to a greater extent than plants do. Plants such as *N. pseudonarcissus* have evolved to tightly regulate the amount of tyramine they produce.

Although the contribution of the remaining partial TyrDC-like sequences awaits further investigation, these results suggest that *Np*TyDC1 is a biochemically defined gatekeeper enzyme that directs L-tyrosine into Amaryllidaceae alkaloid biosynthesis, while providing functional evidence for the divergence of TyDC isoforms in *Narcissus pseudonarcissus* 'King Alfred'.

3. Materials and methods

3.1. Conserved domain search

Two full-length TyDC isoforms from *N. pseudonarcissus* cultivar 'King Alfred' (*Np*TyDC1, GenBank: MF405171; *Np*TyDC2, GenBank: MF405172) were analyzed with the NCBI Conserved Domain Database, with the e-value threshold set to 0.0001 and otherwise default settings. The search focused on verifying the presence of the PLP-dependent decarboxylase domain and identifying the conserved lysine residue required for Schiff base formation. In addition, multiple sequence alignment was carried out using *Np*TyDC1 and *Np*TyDC2 sequences (Table S1) via ClustalW in MEGA (Molecular Evolutionary Genetics Analysis, version 11.0.13) with default parameters.

3.2. Phylogenetic analysis

To evaluate evolutionary relationships, the R 4.4.1 (R Core Team, 2024) and MEGA software were employed to construct a phylogenetic tree. Sequences for the tree were selected by searching all known and characterized decarboxylases that matched *Np*TyDC1 and *Np*TyDC2 in the non-redundant protein sequence database using BlastP, with the parameters max_target_sequence = 500 and e-value = 0.0001. All the hypothetical, unnamed, etc. proteins were excluded, and isomer annotations were consolidated into a single sequence per enzyme per organism (Table S2). Twelve truncated, partial, *Np*TyDC1 or 2 sequences were included in the tree. *Amborella*, the most basal extant angiosperm, was used as the outgroup in the phylogenetic reconstruction (James W. Byng, 2016). The sequences were aligned with ClustalW. Following alignment, a phylogenetic tree was inferred using the BIONJ method from a maximum-likelihood distance matrix under the JTT model. Node support was assessed using 999 bootstrap replicates. The tree was then edited using the Interactive Tree of Life (ITOL interface) (Letunic and Bork, 2024).

3.3. Structural modelling and docking

*Np*TyDC1 and *Np*TyDC2 were modelled as a dimer with the AlphaFold3 server. PLP was covalently linked to Lys321 using MOE2024.09 software's builder (Chemical Computing Group, Québec, Canada) following superimposition with the X-ray crystal structures of *Catharanthus roseus* TDC (*Cr*TDC) in complex with L-tryptophan (PDB:6EEW), *P. somniferum* TyDC (*Ps*TyDC, PDB:6EEM) in complex with L-tyrosine, and *Arabidopsis thaliana* PAAS (*At*PAAS, PDB:6EEI) in complex with L-phenylalanine (Torrens-Spence et al., 2020). MOE software was used to prepare receptors for docking, as outlined by (Lamichhane et al., 2025). Ligand SMILES codes (L-tyrosine, L-tryptophan, L-DOPA, and L-phenylalanine) were obtained from PubChem and cross-referenced with the ZINC20 database (Irwin et al., 2020) to obtained 3D structures for docking. The docking site was predicted using the MOE Site Finder tool, and N(6)-(pyridoxal phosphate)-L-lysine (LLP, lysine covalently linked to PLP) was added by homology. Docking was performed with the AMBER10:EHT force field using Triangle Matcher as the placement method for 200 poses. Flexible and rigid receptor dockings were performed, and the 10 best poses were analyzed. The pose with the best docking score, consistent with the catalytic reaction and closely superimposing with the orthologous crystallized enzyme ligand position, is presented for each ligand. PDB files of docked structures were subsequently submitted to PLIP to identify interactions between ligands and receptor residues (Adasme et al., 2021). Models were then visualized using PyMOL 3.0.0 (Schrödinger, New York, USA).

3.4. Bacterial strains and growth conditions

The bacterial strains used in this study were *Escherichia coli* DH5α (Invitrogen, Thermo Fisher Scientific, ON, Canada), *E. coli* Rosetta (DE3)

pLysS (Novagen, MilliporeSigma Canada Ltd., ON, Canada), and *Agrobacterium tumefaciens* GV3101 (M. Holsters, 1980). The bacteria were cultured in Luria–Bertani (LB) medium supplemented with the appropriate antibiotics under standard growth conditions: *E. coli* strains at 37 °C and *A. tumefaciens* at 28 °C. Antibiotics were used at the following final concentrations (μg mL^{-1}): ampicillin, 100; chloramphenicol, 34; kanamycin, 50; rifampicin, 50; and gentamicin, 30 (all from Fisher Scientific Canada, ON, Canada).

3.5. RNA extraction, cDNA synthesis, and cloning of NpTyDC isoforms

A classical restriction enzyme-based cloning approach was used to construct all desired vectors. Total RNA was extracted from *N. pseudonarcissus* 'King Alfred' (*Np*) bulbs using the cetyltrimethylammonium bromide (CTAB) method as described by Singh and Desgagné-Penix (2017). First-strand cDNA was synthesized from 1 μg of total RNA using the SensiFAST™ cDNA Synthesis Kit (Bioline, Meridian BioScience, Froggabio Inc, ON, Canada) according to the manufacturer's protocol. The open reading frames (ORFs) of *NpTyDC1* and *NpTyDC2* were amplified from bulb cDNA using PrimeSTAR® GXL Premix (TaKaRa Bio, CA, USA) in 50 μL reactions containing 0.2 μM of each forward and reverse primer (Table S3; Integrated DNA Technologies, IO, USA). The PCR cycling conditions were as follows: 98 °C for 2 min (initial denaturation), followed by 35 cycles of 98 °C for 10 s, 55 °C for 20 s, and 72 °C for 1 min, with a final extension at 72 °C for 5 min and an infinite hold at 4 °C. PCR products were analyzed on agarose gels and purified using the GenepHlow™ Gel/PCR Kit (Geneaid, Froggabio). For recombinant protein expression in *Escherichia coli, NpTyDC1* and *NpTyDC2* ORFs were fused in-frame to the C-terminus of the maltose-binding protein (MBP) in the pMAL-c2x vector (New England Biolabs, NEB, ON, Canada). digested with the appropriate enzymes, EcoRI and HindIII for *NpTyDC1*, and BamHI and SalI for *NpTyDC2*, and ligated into the pMAL-c2x vector digested with the same enzyme pairs, using T4 DNA ligase (NEB).

The recombinant plasmids were transformed into chemically competent *E. coli* DH5α cells by heat-shock transformation and plated on LB agar containing ampicillin. Positive clones were screened by colony PCR in 20 μL reactions using Taq DNA polymerase with ThermoPol buffer (NEB) under the following conditions: 95 °C for 5 min, 30 cycles of 95 °C for 30 s, 55 °C for 40 s, and 68 °C for 1 min, followed by a final extension at 68 °C for 5 min. All constructs were confirmed by Sanger sequencing to verify the correct insert orientation and sequence integrity (Génome Québec, QC, Canada).

For subcellular localization studies, *NpTyDC1* and *NpTyDC2* coding sequences were amplified and fused upstream of the yellow fluorescent protein (YFP) gene in the pBTEX binary vector under the control of the CaMV 35S promoter (Majhi et al., 2023). *NpTyDC1* fragments were digested with KpnI and XbaI, while *NpTyDC2* fragments were digested with KpnI and BamHI. Recombinant plasmids were transformed into chemically competent *E. coli* DH5α cells and selected on LB agar plates containing kanamycin. Positive clones were confirmed by colony PCR, and all binary vectors were verified by DNA sequencing prior to further analyses.

3.6. Agrobacterium transformation and transient expression for subcellular localization in Nicotiana benthamiana

The YFP-fusion binary vectors were introduced into *A. tumefaciens* strain GV3101 by electroporation, and transformants were selected on LB agar plates supplemented with rifampicin, kanamycin, and gentamicin at 28 °C. Positive colonies were confirmed by colony PCR. For transient expression assays, *A. tumefaciens* cultures were grown overnight in 5 mL of LB broth containing the same antibiotics at 28 °C with shaking. Cells were harvested by centrifugation at 7900 rcf for 5 min at room temperature, washed three times with 10 mM $MgCl_2$, and resuspended in 5 mL of induction medium (10 mM $MgCl_2$, 10 mM MES [pH 5.6], and 200 μM acetosyringone, Cayman Chemical Co, Cedarlane, ON, Canada). The bacterial suspension was incubated at 28 °C with shaking (200 rpm) for 3–4 h. The *A. tumefaciens* suspension was then adjusted to an optical density of $OD_{600} = 0.25$ with induction medium and infiltrated into the abaxial side of young, fully expanded leaves of five-week-old *Nicotiana benthamiana* plants using a 1 mL needleless syringe. Following agroinfiltration, plants were maintained in a controlled-environment growth chamber under long-day conditions (16 h light/8 h dark) at 22 °C for 48 h.

To visualize the subcellular localization of *Np*TyDC1 and *Np*TyDC2, 48 h post-infiltration, the abaxial epidermis of leaf discs was mounted on microscope slides in a drop of distilled water, covered with a coverslip, and immediately imaged. Protein localization was observed using a confocal laser scanning microscope (Leica TCS SP8; Leica Microsystems, ON, Canada) equipped with a 40×/1.30 oil-immersion objective. Images were initially processed using LAS AF Lite software (Leica Microsystems). CFP was used as a marker control of nucleus and cytoplasmic localization (Kruse et al., 2010). YFP was excited with an argon laser at 488 nm, and fluorescence emission was collected between 500 and 525 nm. CFP was excited with a diode laser at 405 nm, and emission was detected between 420 and 490 nm. Composite images were generated using LAS X software (Leica Microsystems).

3.7. Expression of MBP fusion proteins in E. coli

NpTyDC1 and *NpTyDC2* cloned into the pMAL-c2x vector were transformed using heat shock transformation into chemically competent *E. coli* Rosetta (DE3) pLysS strain for protein expression. Transformed cells were selected on LB plates with ampicillin and chloramphenicol overnight at 37 °C. The positive colonies were screened by colony PCR. A PCR-positive single colony was picked and grown overnight at 37 °C at 220 rpm in 12.5 mL LB broth containing ampicillin and chloramphenicol. The bacteria were then scaled up to flasks containing 200 mL of LB with antibiotics. At an OD of 0.3-0.8, IPTG (Isopropyl β-D-1-thiogalactopyranoside) was added to a final concentration of 0.5 mM (Donovan, 1996). A negative control was also present without any IPTG. After 16 h in the shaker at 18 °C at 150 rpm, cultures were centrifuged at 12,300 rcf at 4 °C for 10 min. The supernatant was discarded and resuspended in a total of 25 mL of binding buffer (1 mM EDTA at pH 8, 150 mM NaCl, 10% glycerol, and 25 mM Tris-HCl at pH 7.5). Each sample was then sonicated for 14 s on and 35 s off at 41 A for 8 min after the addition of 250 μl of phenylmethylsulfonyl fluoride (PMSF, MilliporeSigma), a serine protease inhibitor, and 2 μL of protease inhibitor cocktail (Lively and Powers, 1978). The samples were then centrifuged at 24,100 rcf for 30 min at 4 °C.

3.8. Protein quantification

Protein concentration was determined using the DC Protein Assay (Bio-Rad Laboratories, Inc., ON, Canada). Quantification was performed by measuring absorbance and calculating protein concentration from a standard curve generated using known concentrations of bovine serum albumin (BSA). In each well, 25 μl of reagent A and 5 μl of either the standards or the 1/10-1/20 diluted protein samples were added. After adding 200 μl of reagent B, the plate was covered with foil and incubated at room temperature for 30 min. The OD_{750} was measured using a Synergy H1 Biotek plate reader (VT, USA), and the concentration was calculated using the concentration curve of the BSA samples in Microsoft Excel with the formula $x = \frac{y-b}{a}$. The final concentration was then calculated by multiplying the result by the dilution factor.

3.9. SDS-PAGE

Considering the predicted molecular weight of the tagged recombinant protein (~100 kDa), an 8% sodium dodecyl sulfate (SDS)–

polyacrylamide gel was prepared. Each sample had 50 μg of protein in a final volume of 30 μl, to which 7.5 μl of Laemmli 4x buffer (Bio-Rad Laboratories, Inc.) was added. Electrophoresis was first conducted at 80 V until the samples exited the stacking gel; thereafter, the voltage was increased to 120 V and maintained for 2 h. Protein bands were visualized using Coomassie Blue staining. Following staining, excess dye was removed by incubating the gel in water overnight prior to imaging.

3.10. Protein purification and desalination

Following cell lysis by sonication, the lysates were clarified twice at 4 °C to remove cell debris, and the soluble fraction was gently mixed with amylose resin beads (NEB). The target proteins were retained on the column matrix, while non-binding proteins were washed away with column buffer. Bound MBP–*Np*TyDC1 and MBP–*Np*TyDC2 were then released using 10 mM maltose, and the flow-through, wash, and elution fractions were examined by SDS-PAGE to confirm the expected ~100 kDa bands. For the enzymatic assay, the maltose-containing eluates were desalted and exchanged into 150 mM Tris-HCl (pH 8.0) using MilliporeSigma Amicon Ultra centrifugal filter tubes. Several rounds of dilution and reconcentration ensured efficient removal of small molecules and salts. The final protein preparations were quantified by BSA assay as described earlier, divided into aliquots, flash-frozen in liquid nitrogen, and stored at −80 °C until further use.

3.11. Enzymatic assays

Enzymatic assays were performed in 100 μL reaction volumes containing purified recombinant protein, substrate, PLP, and Tris–HCl buffer (pH 8.0). For each assay, two negative controls were included, one lacking enzyme and one lacking substrate. Experiments were performed in triplicate and analyzed using high-performance liquid chromatography (HPLC) coupled with tandem mass spectrometry (MS/MS). Substrate specificity of *Np*TyDC1 and *Np*TyDC2 was first analyzed to identify products formed from individual aromatic amino acids. Optimization experiments were conducted only for *Np*TyDC1, as this isoform was selected for further characterization based on the outcome of substrate specificity assays. Enzymatic assays were optimized in a stepwise manner. A common set of baseline conditions was used at the start, and each experimental parameter was then examined individually. After each experiment, the conditions identified as optimal were carried forward and used as fixed settings for the next assay. At each step, only the parameter being studied was changed. Reaction duration was set to 80 min, and the enzyme amount was 30 ng per 100 μL reaction in the final experiment assessing substrate concentration. Before the optimization, a substrate specificity assay was performed using L-tyrosine, L-phenylalanine, L-tryptophan, and L-DOPA as individual substrates. The reaction temperature was varied at five levels in triplicate. Purified *Np*TyDC1 was tested beginning at 120 ng per 100 μL reaction, followed by serial dilutions down to 0.234 ng. L-tyrosine concentrations ranged from 0.046 mM to 0.15 mM in triplicate. The reaction duration was optimized by repeating the enzymatic assay under identical conditions and stopping each reaction at specified time points, ranging from 10 to 720 min.

Statistical analyses were performed using R 4.4.1. The effects of temperature, enzyme concentration, reaction time, and substrate concentration on tyramine formation were then examined in sequence. Dilution factors were incorporated, and the molecular weight of each molecule was used to convert concentrations from ng/mL to μM across all analyses. Statistical significance was assessed using either three-way or one-way ANOVA, followed by Tukey's test. Trends in tyramine production were analyzed using local weighted smoothing (loess) fit to identify optimal ranges, linear response regions, and saturation behaviour.

Initial velocities were calculated from tyramine formation over the 80-min incubation. Results were summarized using the *get* package version 1.0.0 (Iannone et al., 2025), and dose–response relationships were visualized by plotting tyramine formation against tyrosine concentration. We integrated the time course and substrate range data to determine Michaelis–Menten parameters. For the time-course, we focused on the 0-40-min window, added a $t = 0$ point with zero product for each replicate, and fit linear regressions of tyramine concentration versus time to obtain v_0 values. We combined these points with the v_0 values from the substrate series and fit the Michaelis–Menten equation by nonlinear regression, estimating V_{max} and K_m for both the substrate-only and combined datasets. We calculated *kcat* by converting V_{max} to micromolar per second and normalizing them by enzyme concentration.

3.12. HPLC-MS/MS analysis

An HPLC-MS/MS system equipped with an Agilent Jet Stream ionization source, a binary pump, an autosampler, and a column compartment (Agilent Technologies, Santa Clara, California, USA) was used for the analysis. Compound separation was achieved using a Kinetex EVO C18 column (150 × 4.6 mm, 5 μm, 100 Å; Phenomenex, Torrance, USA). Five microliters of each sample were injected onto the column that was set at 30 °C. A gradient method made of (A) formic acid 0.1% v/v in Milli-Q water and (B) formic acid 0.1% v/v in methanol with a flow rate of 0.4 mL/min was used to achieve chromatographic separation. The HPLC elution program is described as follows: 0 min, 10% B; 10.0 min, 10% B; 20.0 min, 100% B; 25.0 min, 100% B; 26.0 min, 10% B. The total run time was 30 min per sample to allow the reconditioning of the column prior to the next injection. The parameters used in the MS/MS source were set as follows: gas flow rate 10 L min^{-1}, gas temperature 300 °C, nebulizer 45 psi, sheath gas flow 11 L min^{-1}, sheath gas temperature 300 °C, capillary voltage 4000 V in ESI+ and 3500 V in ESI- and nozzle voltage 500 V. Agilent MassHunter Data Acquisition (version 1.2) software was used to control the HPLC-MS/MS. MassHunter Qualitative Analysis (version 10.0) and MassHunter Quantitative QQQ Analysis (version 10.0) software were used for data processing. Compound identifications were made using authentic reference standards in MRM mode for kinetic study and enzyme assay optimization or by using Single Ion Monitoring (SIM) mode and Product Ion (PI) mode to generate collision-induced dissociation (CID) mass spectra for substrate specificity assays. MRM transitions and instrument parameters used for identifications in kinetic study and enzyme assays optimization (*i.e.,* temperature, substrate concentration, time, and enzyme concentration) experiments are included in Table S4. Instrument parameters used in SIM and in PI modes to obtain the full CID mass spectrum of signals detected are presented in Table S5 and Table S6 respectively. Standard calibration curves were prepared as follows: Two working solutions were prepared containing L-tyrosine (L-TYR) and tyramine (TYR) at 10 mg/L in mobile phase solution (*i.e.,* Milli-Q water and methanol (90:10), both containing 0.1% formic acid). These solutions were further diluted to prepare calibration solutions with the following concentrations in triplicate: 0, 12.5, 25, 50, 100, 200, 1000, and 5000 ng/mL. Internal standard papaverine was added at a constant concentration of 1000 ng/mL in each calibration solution. These standard solutions were injected into the HPLC-MS/MS system and used to generate calibration curve regressions. Fig. S1 and Fig. S2 show the calibration curves obtained by plotting the area ratio (*i.e.,* analyte's peak area divided by internal standard's peak area) obtained as a function of the analyte's concentration, which allowed L-TYR and TYR quantification for all enzymatic assays. Following analysis, reported values represent HPLC-DAD peak area ratios normalized to the internal standard papaverine. Because substrates like tyramine and phenylethylamine have different UV absorption coefficients, their detector response factors relative to the internal standard differ; consequently, area ratios cannot be compared across different products within the same enzyme.

4. Conclusion

This study defines the biochemical properties of tyrosine decarboxylase isoforms from *Narcissus pseudonarcissus* 'King Alfred', a genus renowned for producing pharmacologically important Amaryllidaceae alkaloids. *Np*TyDC1 functions as a gatekeeping enzyme that converts L-tyrosine to tyramine and exhibits constrained catalytic turnover, consistent with regulatory control at the entry point of alkaloid biosynthesis rather than sustained high metabolic flux.

The phylogenetic separation of *Np*TyDC1 and *Np*TyDC2 is mirrored by their distinct biochemical behaviours. *Np*TyDC1 displays strong specificity for L-tyrosine in enzymatic assays, whereas *Np*TyDC2 lacks detectable tyrosine decarboxylase activity under the same conditions, providing functional evidence that these isoforms have diverged rather than retained redundant roles. Together, these findings suggest that *Np*TyDC1 is a biochemically defined gatekeeper of Amaryllidaceae alkaloid biosynthesis, among the characterized isoforms, and provide a framework for understanding the functional diversification of aromatic amino acid decarboxylases in this family. Full-length sequencing and functional characterization of the remaining partial TyDC-like transcripts will be necessary to fully delineate the enzymatic network directing carbon flux into Amaryllidaceae alkaloid biosynthesis in *N. pseudonarcissus*.

Funding

This research was financially supported by the Canada Research Chairs on plant specialized metabolism Award No CRC-2023-00353 to I. D-P. Thanks are extended to the Canadian taxpayers and to the Canadian government for supporting the Canada Research Chairs Program.

CRediT authorship contribution statement

Arghavan Arjmandi: Conceptualization, Data curation, Formal analysis, Investigation, Validation, Visualization, Writing – original draft, Writing – review & editing. **Bharat Bhusan Majhi:** Conceptualization, Formal analysis, Investigation, Methodology, Resources, Writing – review & editing. **Natacha Mérindol:** Conceptualization, Project administration, Resources, Validation, Visualization, Writing – review & editing. **Sarah-Eve Gélinas:** Investigation, Methodology, Validation, Writing – review & editing. **Karen Cristine Gonçalves dos Santos:** Data curation, Formal analysis, Software, Visualization, Writing – review & editing. **Isabella Burgos-Holguin:** Investigation, Methodology, Writing – review & editing. **Yasmin Moreto Guaitolini:** Investigation, Methodology, Writing – review & editing. **Patrick Lagüe:** Resources, Software, Writing – review & editing. **Isabel Desgagné-Penix:** Conceptualization, Funding acquisition, Project administration, Resources, Supervision, Validation, Visualization, Writing – review & editing.

Declaration of competing interest

The authors declare the following financial interests/personal relationships which may be considered as potential competing interests: Isabel Desgagne-Penix reports financial support was provided by Canada Research Chairs Program. If there are other authors, they declare that they have no known competing financial interests or personal relationships that could have appeared to influence the work reported in this paper.

Acknowledgement

We thank all members of our research team, as well as Professor Hugo Germain and his team, for insightful discussions and for their scientific, technical, and collegial support.

Appendix A. Supplementary data

Supplementary data to this article can be found online at https://doi.org/10.1016/j.phytochem.2026.115017.

Data availability

Data will be made available on request.

References

Adasme, M.F., Linnemann, K.L., Bolz, S.N., Kaiser, F., Salentin, S., Haupt, V.J., Schroeder, M., 2021. Plip 2021: expanding the scope of the protein–ligand interaction profiler to DNA and RNA. Nucleic Acids Res. 49, W530–W534.

Byng, James W., M. W. C, Christenhusz, Maarten J.M., Fay, Michael F., Judd, Walter S., Mabberley, David J., Sennikov, Alexander N., Soltis, Douglas E., Soltis, Pamela S., Stevens, Peter F., 2016. An update of the angiosperm phylogeny group classification for the orders and families of flowering plants. Bot. J. Linn. Soc. 181, 1–20.

Cortes, N., Alvarez, R., Osorio, E.H., Alzate, F., Berkov, S., Osorio, E., 2015. Alkaloid metabolite profiles by GC/MS and acetylcholinesterase inhibitory activities with binding-mode predictions of five Amaryllidaceae plants. J. Pharm. Biomed. Anal. 102, 222–228.

Desgagné-Penix, I., 2021. Biosynthesis of alkaloids in Amaryllidaceae plants: a review. Phytochem. Rev. 20, 409–431.

Donovan, C.R.a.B.G., 1996. Review: optimizing inducer and culture conditions for expression of foreign proteins under the control of the lac promoter. J. Ind. Microbiol. 16, 145–154.

Facchini, P.J., Johnson, A.G., Poupart, J., De Luca, V., 1994. Expression in Escherichia coli and partial characterization of two tyrosine/dopa decarboxylases from opium poppy. Phytochemistry 38, 1119–1126.

Facchini, P.J., De Luca, V., 1994. Differential and tissue-specific expression of a gene family for tyrosine/dopa decarboxylase in opium poppy. J. Biol. Chem. 269, 26684–26690.

Georgiev, V., Ivanov, I., Pavlov, A., 2020. Recent progress in Amaryllidaceae biotechnology. Molecules 25.

Holsters, M., B. S, 1980. The functional organization of the Nopaline A. tumerfaciens plasmid pTiC58. Plasmid 3, 212–230.

Hotchandani, T., de Villers, J., Desgagne-Penix, I., 2019. Developmental regulation of the expression of Amaryllidaceae alkaloid biosynthetic genes in Narcissus papyraceus. Genes 10.

Hu, J., Li, W., Liu, Z., Zhang, G., Luo, Y., 2021. Molecular cloning and functional characterization of tyrosine decarboxylases from galanthamine-producing Lycoris radiata. Acta Physiol. Plant. 43.

Iannone, R., Cheng, J., Schloerke, B., Hughes, E., Lauer, A., Seo, J., Brevoort, K.R.O., 2025. Gt: Easily Create Presentation-Ready Display Tables.

Irwin, J.J., Tang, K.G., Young, J., Dandarchuluun, C., Wong, B.R., Khurelbaatar, M., Moroz, Y.S., Mayfield, J., Sayle, R.A., 2020. ZINC20-A free ultralarge-scale chemical database for ligand discovery. J. Chem. Inf. Model. 60, 6065–6073.

Ka, S., Merindol, N., Sow, A.A., Singh, A., Landelouci, K., Plourde, M.B., Pépin, G., Masi, M., Di Lecce, R., Evidente, A., Seck, M., Berthoux, L., Chatel-Chaix, L., Desgagné-Penix, I., 2021. Amaryllidaceae alkaloid cherylline inhibits the replication of dengue and zika viruses. Antimicrob. Agents Chemother. 65, e0039821.

Kawalleck, P., Keller, H., Hahlbrock, K., Scheel, D., Somssich, I.E., 1993. A pathogen-responsive gene of parsley encodes tyrosine decarboxylase. J. Biol. Chem. 268, 2189–2194.

Kilgore, M.B., Augustin, M.M., Starks, C.M., O'Neil-Johnson, M., May, G.D., Crow, J.A., Kutchan, T.M., 2014. Cloning and characterization of a norbelladine 4′-O-Methyltransferase involved in the biosynthesis of the Alzheimer's drug galanthamine in Narcissus sp. aff. pseudonarcissus. PLoS One 9, e103223.

Kilgore, M.B., Holland, C.K., Jez, J.M., Kutchan, T.M., 2016. Identification of a noroxomaritidine reductase with Amaryllidaceae alkaloid biosynthesis related activities. J. Biol. Chem. 291, 16740–16752.

Koirala, M., Merindol, N., Karimzadegan, V., Gélinas, S.-E., Liyanage, N.S., Lamichhane, B., Tobón, M.C.G., Lagüe, P., Desgagné-Penix, I., 2024. Kinetic and in silico structural characterization of norbelladine O-methyltransferase of Amaryllidaceae alkaloids biosynthesis. J. Biol. Chem. 300, 107649.

Kruse, T., Gehl, C., Geisler, M., Lehrke, M., Ringel, P., Hallier, S., Hansch, R., Mendel, R. R., 2010. Identification and biochemical characterization of molybdenum cofactor-binding proteins from Arabidopsis thaliana. J. Biol. Chem. 285, 6623–6635.

Lamichhane, B., Gelinas, S.E., Merindol, N., Koirala, M., Dos Santos, K.C.G., Germain, H., Desgagne-Penix, I., 2025. Elucidating the enzyme network driving Amaryllidaceae alkaloids biosynthesis in Leucojum aestivum. Plant Biotechnol. J. 23, 1988–2005.

Lehmann, T., Pollmann, S., 2009. Gene expression and characterization of a stress-induced tyrosine decarboxylase from Arabidopsis thaliana. FEBS Lett. 583, 1895–1900.

Letunic, I., Bork, P., 2024. Interactive tree of life (iTOL) v6: recent updates to the phylogenetic tree display and annotation tool. Nucleic Acids Res. 52, W78–W82.

Li, Y., Guo, B., Yang, J., Li, Y., Chen, B., Zheng, Y., 2025. Physiological and molecular regulation of Amaryllidaceae alkaloid biosynthesis in lycoris species. Russ. J. Plant Physiol. 72.

Li, Y., Wang, Y., Huang, L., Chen, C., An, N., Zheng, X., 2022. Identification and functional characterization of tyrosine decarboxylase from Rehmannia glutinosa. Molecules 27.

Lively, M.O., Powers, J.C., 1978. Specificity and reactivity of human granulocyte elastase and Cathepsin G, porcine pancreatic elastase, bovine chymotrypsin and trypsin toward inhibition with sulfonyl fluorides. Biochim. Biophys. Acta 525, 171–179.
Luaces, P., Sánchez, R., Expósito, J., Pérez-Pulido, A.J., Pérez, A.G., Sanz, C., 2024. Functional and physiological characterization of tyrosine decarboxylases from Olea europaea L. involved in the synthesis of the main phenolics in olive fruit and virgin olive oil. Int. J. Mol. Sci. 25.
Majhi, B.B., Gélinas, S.E., Mérindol, N., Ricard, S., Desgagné-Penix, I., 2023. Characterization of norbelladine synthase and noroxomaritidine/norcraugsodine reductase reveals a novel catalytic route for the biosynthesis of Amaryllidaceae alkaloids including the Alzheimer's drug galanthamine. Front. Plant Sci. 14, 1231809.
Moreno-Arribas, V., Lonvaud-Funel, A., 1999. Tyrosine decarboxylase activity of Lactobacillus brevis IOEB 9809 isolated from wine and L. brevis ATCC 367. FEMS (Fed. Eur. Microbiol. Soc.) Microbiol. Lett. 180, 55–60.
Ptak, A., Warchol, M., Moranska, E., Laurain-Mattar, D., Spina, R., Dupire, F., Waligorski, P., Simlat, M., 2026. Amaryllidaceae alkaloids and phenolic acids identification in Leucojum aestivum L. plant cultures exposed to different temperature conditions. Molecules 31.
R Core Team, 2024. R: a Language and Environment for Statistical Computing. R Foundation for Statistical Computing.
Sandmeier, E., Hale, T., Christen, P., 1994. Multiple evolutionary origin of pyridoxal-5'-phosphate-dependent amino acid decarboxylases. Eur. J. Biochem. 221, 997–1002.
Singh, A., Massicotte, M.A., Garand, A., Tousignant, L., Ouellette, V., Berube, G., Desgagne-Penix, I., 2018. Cloning and characterization of norbelladine synthase catalyzing the first committed reaction in Amaryllidaceae alkaloid biosynthesis. BMC Plant Biol. 18, 338.
Singh, A., Desgagné-Penix, I., 2017. Transcriptome and metabolome profiling of Narcissus pseudonarcissus 'King Alfred' reveal components of Amaryllidaceae alkaloid metabolism. Sci. Rep. 7.
Torrens-Spence, M.P., Chiang, Y.C., Smith, T., Vicent, M.A., Wang, Y., Weng, J.K., 2020. Structural basis for divergent and convergent evolution of catalytic machineries in plant aromatic amino acid decarboxylase proteins. Proc. Natl. Acad. Sci. U. S. A. 117, 10806–10817.
Torrens-Spence, M.P., Gillaspy, G., Zhao, B., Harich, K., White, R.H., Li, J., 2012. Biochemical evaluation of a parsley tyrosine decarboxylase results in a novel 4-hydroxyphenylacetaldehyde synthase enzyme. Biochem. Biophys. Res. Commun. 418, 211–216.
Torrens-Spence, M.P., Liu, P., Ding, H., Harich, K., Gillaspy, G., Li, J., 2013. Biochemical evaluation of the decarboxylation and decarboxylation-deamination activities of plant aromatic amino acid decarboxylases. J. Biol. Chem. 288, 2376–2387.
Tousignant, L., Diaz-Garza, A.M., Majhi, B.B., Gélinas, S.-E., Singh, A., Desgagne-Penix, I., 2022. Transcriptome analysis of Leucojum aestivum and identification of genes involved in norbelladine biosynthesis. Planta 255, 30.
Wang, R., Han, X., Xu, S., Xia, B., Jiang, Y., Xue, Y., Wang, R., 2019. Cloning and characterization of a tyrosine decarboxylase involved in the biosynthesis of galanthamine in Lycoris aurea. PeerJ 7, e6729.
Zhang, K., Ni, Y., 2014. Tyrosine decarboxylase from Lactobacillus brevis: soluble expression and characterization. Protein Expr. Purif. 94, 33–39.
Zhu, H., Xu, G., Zhang, K., Kong, X., Han, R., Zhou, J., Ni, Y., 2016. Crystal structure of tyrosine decarboxylase and identification of key residues involved in conformational swing and substrate binding. Sci. Rep. 6, 27779.